Progress In Electromagnetics Research C, Vol. 127, 31–48, 2022

Preamble-Based Synchronization for Communication-Assisted Chirp Sequence Radar

Mohamad B. Alabd*, Benjamin Nuss, Lucas G. de Oliveira, Yueheng Li, Axel Diewald, and Thomas Zwick

Abstract—Chirp sequence has been adopted in automotive applications for its simple generation and flexible integration within radar-centric systems. Besides, recent studies have shown its ability to carry data between communicating vehicles in the surroundings. Since the parameters adopted from current automotive radar sensors can differ at the transmitter side dependent on the automotive supplier, the carrier alignment of the communication receiver of one of the communicated nodes might not concur with the one in the transmitter. This paper presents a novel two-stage synchronization method for communication-assisted chirp sequence (CaCS) signals. The proposed synchronization method applies a sequence of up- and down-chirp as a preamble to estimate frequency and time offsets during the transmission. The suggested synchronization scheme supports partial chirp modulation systems and can be adapted for similar radar-centric systems that employ chirp modulation. The former stage performs a coarse synchronization, reallocates the receive carrier frequency, and corrects eventual time offsets between the communication receiver from one CaCS-node and the transmitter of another node. The carrier allocation at the communication receiver side is based on a combination of spectrum sensing via short-time Fourier transforms and image processing to estimate the transmitting signal pattern (slope, frequency offset, and delay). The latter stage, in its turn, relies on range-Doppler estimation to perform a fine correction of time and frequency offsets and compensates residual offsets of the coarse synchronization stage. Furthermore, the paper analyzes the case of a multi-user scenario with mutual interference between the signals that affects the synchronization and communication data detection. Besides, measurements are provided based on two completely unsynchronized software-defined radios to validate the proposed method. The study also illustrates the influence of the signal-to-noise ratio on the proposed method and verifies it with simulations in MATLAB. As a result, the offsets at the investigated CaCS-node are returned to recover the transmitted data correctly.

1. INTRODUCTION

Current radar sensors employ chirp sequence (CS) waveforms in automotive applications to detect various targets in the surroundings [1–3]. This employment spares the expense of the design and eases the manufacturing compared with other proposed waveforms in the literature (e.g., orthogonal frequency-division multiplexing (OFDM) and phase-modulated continuous-wave (PMCW)). However, the sensors share the same frequency spectrum, leading to a high possibility of mutual interference between the operated radar sensors [4–7]. In this framework, the integration of communication data within radar systems can be employed to avoid interference events between radar sensors and is responsible for exchanging vital signal parameters (e.g., the utilized bandwidth, the signal duration, and the center frequency) so that different radar signals will not overlap in time or frequency.

Received 22 July 2022, Accepted 14 October 2022, Scheduled 25 November 2022

* Corresponding author: Mohamad Basim Alabd (basim.alabd@kit.edu).

The authors are with the Institute of Radio Frequency Engineering and Electronics (IHE), Karlsruhe Institute of Technology (KIT), Karlsruhe 76131, Germany.

Most published studies related to shared radar communication systems are limited to system-based models that perform communication features through an external system specified only for this purpose. Vehicle-to-vehicle (V2V), vehicle-to-infrastructure (V2I), and vehicle to roadside (V2R) are frequent examples of this approach that employs a separated communication link [8, 9]. In this context, vehicle-to-everything (V2X) techniques cover V2V, V2I, and V2R by accessing a specific centralized network such as 5G in telecommunication architectures to allow communication between the nodes in the environment [10]. In addition, Intelligent Transport System (ITS-G5) is also a prominent candidate for enabling communication between vehicles. It is related to the efficient employment of a decentralized WLAN (IEEE802.11p) in a dynamic automotive environment [11]. All the aforementioned systems based on 5G networks, or ITS-G5, can achieve an appropriate data rate for different communication purposes independent of the radar signals. Besides, the synchronization between the nodes or the vehicles in all mentioned systems depends on an additional scheme utilized for communication as well as an external source for accurate time synchronization, such as the Global Positioning System (GPS) and Global Navigation Satellite System (GNSS) [12, 13].

Apart from that, signal-based systems modulate communication data within the transmitting radar signals without using additional equipment for synchronization resulting in joint radar-communication (RadCom) systems [14, 15] or dual-function radar communication (DFRC) systems [16]. A common approach for such systems is the orthogonal frequency-division multiplexing (OFDM), which has gained prominence in research regarding its convenient signal processing for communication and radar sensing [17, 18]. Another promising approach for joint radar communications is orthogonal chirp division multiplexing (OCDM) [19, 20], which relies on the modulation of orthogonal subchirps instead of subcarriers compared with OFDM. Both OFDM and OCDM systems can efficiently perform time-frequency synchronization based on preamble techniques, such as Schmidl and Cox [21, 22]. However, both schemes require fast analog-to-digital converters (ADCs) with sampling rates above 1 GHz to satisfy the range resolution requirement in automotive radar applications. The demand of having fast ADCs is a prominent drawback regarding the costs compared with current radar sensors in the automotive sector, which only exploit about 20 MHz [23] at the receiver side. In contrast to the aforementioned digital modulation schemes, the possibility of integrating communication facilities in frequency-modulated continuous-wave (FMCW) or chirp sequence signals is investigated in [24–28] as communication-assisted chirp sequence (CaCS) systems. In this framework, enabling the communication link between the vehicles can assist their radar functionality and achieve an appropriate data rate for specific purposes (e.g., mitigate the mutual interference). Based on CaCS systems, a possible integration for the communications symbols within the chirp signal is the partial chirp modulation technique introduced in [29]. The mentioned CaCS system satisfies the hardware requirements and an appropriate data rate for the automotive scenarios. In this context, a separate communication receiver is needed at the receiver node, or the radar receiver should be able to switch between the two functionalities. However, the study in [29] does not investigate synchronization methods between the communicating vehicles during the transmission.

In [30], the authors introduced a synchronization method for phase-coded FMCW (PC-FMCW) automotive radars, which solely achieves fine synchronization features between communication-assisted radar nodes that are already coarsely synchronized via GPS. Aiming to perform a chirp-like [31, 32] synchronization scheme within a practicable large bandwidth and the possible absence of GPS signals between CaCS-nodes, this paper introduces a novel two-stage time-frequency synchronization method for CaCS systems. The former stage relies on coarse timing synchronization related to the correlation of a sliding preamble (constituted by up-and down-chirps) and time-frequency analyses (image processing) of the preamble within a narrow band derived from the signal. The time-frequency analyses involve short-time Fourier transforms (STFT) with thresholding and linear regression on the thresholded time-frequency plane after STFT to estimate coarse time and frequency offsets between the transmitter of one CaCS-node and the communication receiver of another node. The second synchronization step is employed to control fine time and frequency offsets that might not be corrected within the coarse stage because of residuals errors of the applied linear regression in the previous step. As an extension to the study in [29], this paper presents a detailed description of a CaCS system model. It is designed based on a limited filter bandwidth applied at the communication receiver of one investigated node. Therefore, the achieved data rate will be limited compared to the RadCom systems based on digital modulation

schemes. Besides, the study was taken under the assumption of having a dominant line-of-sight (LOS) path, where the multiple-path case has limited effects for automotive scenarios [33].

The remainder of this study is organized as follows. The system model of a CaCS system is described with typical time and frequency offsets between two nodes in Section 2. In addition, Section 3 details the waveform structure used in the transmitter, and Section 4 outlines the receiving procedure with an initiative insight for the case of a scenario with multiple signals. In Section 5, the measurement setup and obtained results are presented. Finally, the concluding remarks can be found in Section 6.

2. SYSTEM MODEL

Based on the chirp sequence radar presented in [34, 35], the representation of a chirp in the time domain and duration T_{C}, bandwidth B and initial phase φ_0 can be described as

$$s\left(t\right) = A\exp\left\{\mathrm{j}\left[\pi\mu t^2 + 2\pi\left(f_{\mathrm{C}} - \frac{B}{2}\right)t + \varphi_0\right]\right\} \tag{1}$$

where f_{C} is the carrier frequency, and $\mu = B/T_{\mathrm{C}}$ represents the chirp rate. A sequence of multiple modulated chirps $Q_{\mathrm{rc}} \in \mathbb{N}_+$ with index $q_{\mathrm{rc}} \in \{0, 1, \ldots, Q_{\mathrm{rc}}-1\}$ and equal pauses is transmitted to enable relative speed estimation at the radar receiver side. An exemplary modulated chirp sequence with time repetition interval T_{RRI} and a duration of $T_{\mathrm{Seq}}^{\mathrm{rc}} = Q_{\mathrm{rc}}T_{\mathrm{RRI}}$ is depicted in Fig. 1 in accordance to the study in [29]. In the time domain, the representation of a modulated chirp can be characterized by (2), where B_{Mod} is the modulated bandwidth, and T_{Com} is the duration of the communication section. $f_{\mathrm{Com,Tx}}$ is the communication center frequency at the transmitter side, and $\varphi_{\mathrm{Mod}}(t) \in \{\pi/4, 3\pi/4, 5\pi/4, 7\pi/4\}$ denotes the phase related to the quadrature phase shift keying (QPSK) modulation. It is worth highlighting that the aforementioned modulation can be replaced by another conventional digital modulation schemes, e.g., ASK or FSK.

$$s_{\mathrm{Mod}}\left(t\right) = \begin{cases} A\exp\left\{\mathrm{j}\left[\pi\mu t^2 + 2\pi\left(f_{\mathrm{C}} - \frac{B}{2}\right)t + \varphi_0\right]\right\} & \text{if} \\ 0 \le t < T_{\mathrm{C}} - T_{\mathrm{Com}} & \\ A\exp\left\{\mathrm{j}\left[\pi\mu(t-(T_{\mathrm{C}}-T_{\mathrm{Com}}))^2 + 2\pi\left(f_{\mathrm{Com,Tx}} - \frac{B_{\mathrm{Mod}}}{2}\right)(t-(T_{\mathrm{C}}-T_{\mathrm{Com}})) + (\varphi_0 + \varphi_{\mathrm{Mod}}(t))\right]\right\} & \text{if} \\ T_{\mathrm{C}} - T_{\mathrm{Com}} \le t < T_{\mathrm{C}} & \end{cases} \tag{2}$$

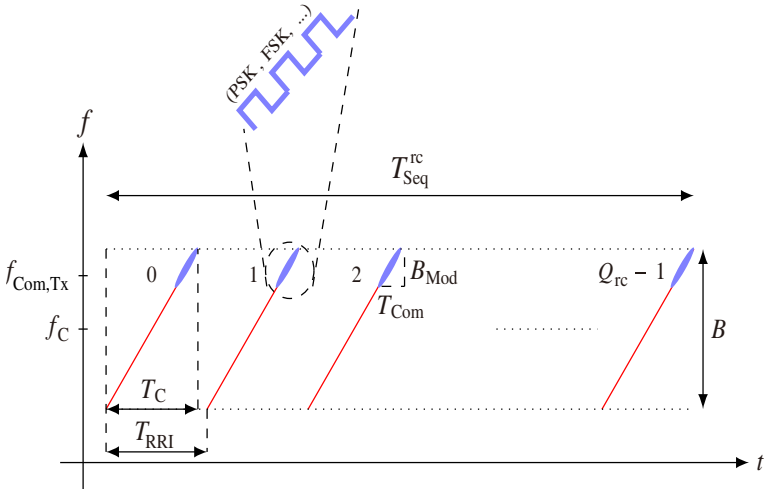

Figure 1. Partially modulated chirps of the communication-assisted radar scheme. The blue-colored part presents the modulated section of each chirp. T_{C} is the chirp duration, T_{RRI} is the ramp repetition interval and $T_{\mathrm{Seq}}^{\mathrm{rc}}$ is the sequence duration. B is the signal bandwidth, B_{Mod} is the modulated bandwidth, and $f_{\mathrm{Com,Tx}}$ is the communication center frequency.

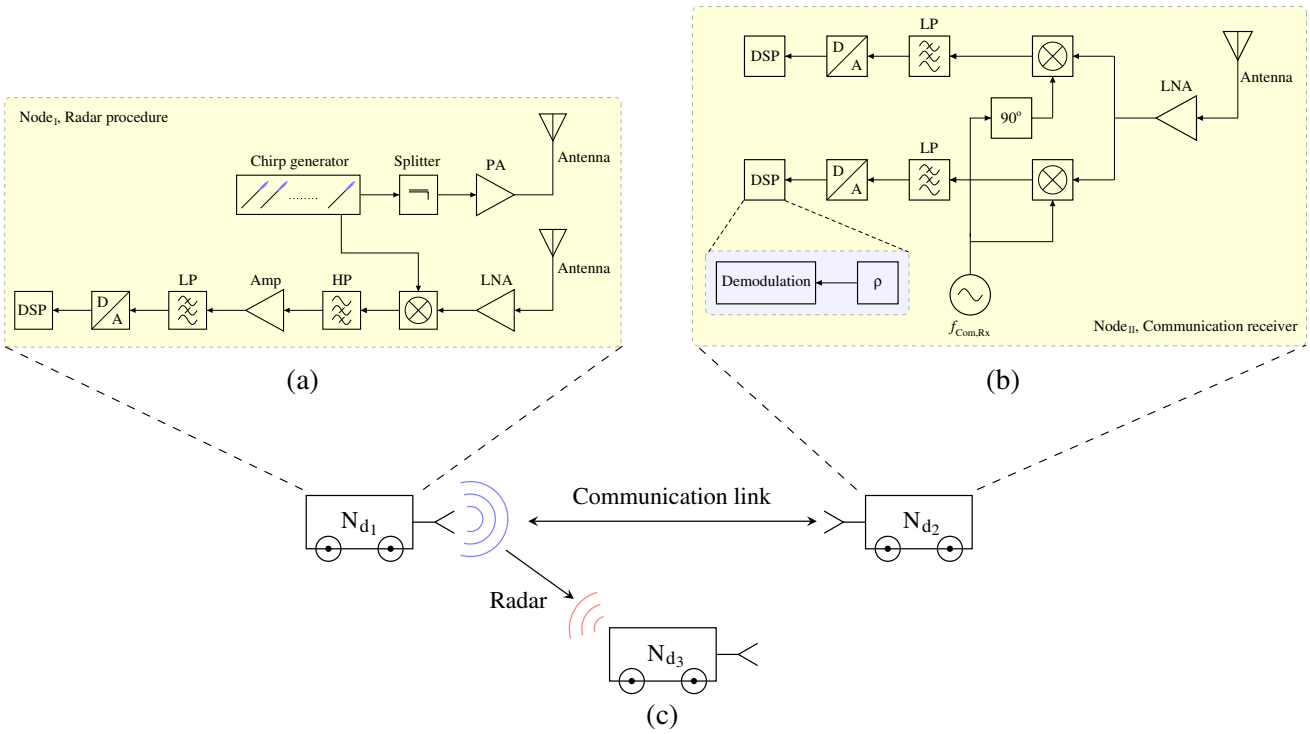

Figure 2. Block diagram of CaCS nodes in automotive scenarios. N_{d_1} represents the node that is responsible for radar measurements. N_{d_2} is the node where the valuation of communication data takes place. N_{d_3} illustrates a possible target in the surroundings. (a) Radar transceiver at N_{d_1}. (b) Communication receiver at N_{d_2}. (c) Exemplary scenario in automotive applications.

Figure 2 illustrates an exemplary scenario in automotive applications. N_{d_1} represents the node that conducts the radar measurements; N_{d_2} depicts the receiver that evaluates the communication data; and N_{d_3} acts as a possible target in the environment. The chirp signal at N_{d_1} is generated mainly by an oscillator and a phase-locked loop (PLL). This compound is simplified as a chirp generator in the block diagram of the transmitter in Fig. 2(a). In this context, the hardware design of current radar sensors should require only minor changes to modulate the communication data onto every transmitted chirp. Those changes are related to the modulation of communication data within the upper part of every chirp, dependent on the technology used in current PLLs [36]. The resulting signal passes through a splitter and undergoes amplification by a power amplifier (PA) before being radiated by the transmit antenna. At the radar receiver side of N_{d_1}, the reflected signal, in its turn, undergoes amplification by a low-noise amplifier (LNA). Next, the amplified signal is mixed with the transmitting signal, and the result undergoes high-pass (HP) filtering to eliminate the coupling between transmitting and receiving antennas. The baseband signal is amplified afterward and filtered by a low-pass (LP) to limit the required sampling rate used in the digital domain for further signal processing steps and detect the targets in the environment. The target detection depends on the 2D-FFT radar signal processing, as described in [37].

The main advantage of the recommended communication approach in [29] is that only minor changes are necessary to adjust the transmitter, and solely a narrow bandwidth is employed at the communication receiver of one CaCS-node. For this reason, the requirement of having fast ADCs is avoided compared with digital modulation schemes such as OFDM, and a simple platform with an appropriate sampling rate can be adopted for the CaCS-nodes. Fig. 2(b) depicts the communication receiver block diagram. The receiving signal undergoes amplification by an LNA and is then downconverted with the communication carrier frequency, filtered by an LP filter, and converted to the digital domain by an ADC. As the study in [29] explains, a part of the transmitting chirp is used as a preamble. This preamble is known at the receiver and differs from the aforementioned counterpart

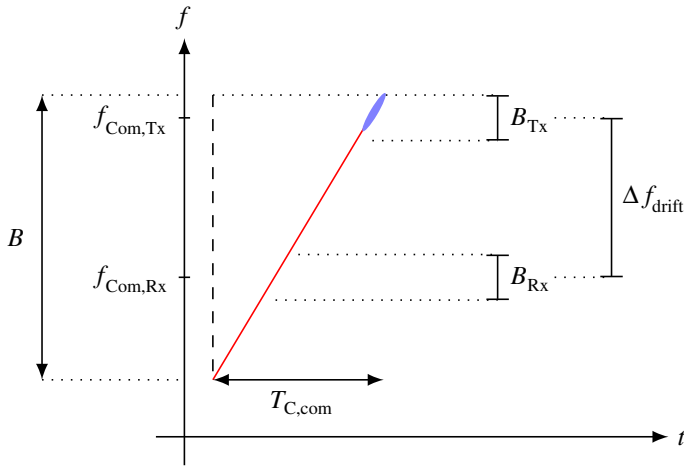

Figure 3. Exemplary frequency difference $\Delta f_{\mathrm{drift}}$ between the carrier frequencies at the transmitter and receiver side related to one CaCS scheme.

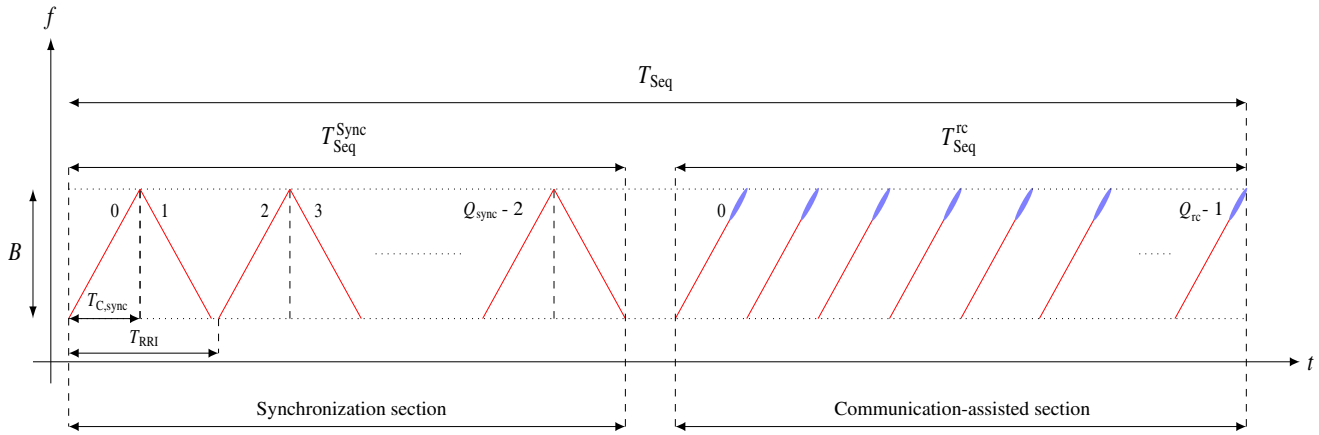

Figure 4. Structure of the transmitted CaCS signal, including the pattern of the coarse, fine synchronization chirps, the dedicated chirps for both radar and communication.

depicted in Fig. 4 and Fig. 5 in the next section. The receiving signal is cross-correlated with the chosen preamble, and the maximum peak at the correlator output is extracted to indicate the start of the communication section. Consequently, the demodulation is implemented based on the digital modulation constellation used for the modulated part of the chirps. It is worth highlighting that an in-phase quadrature (IQ) receiver is adopted to demodulate different digital constellations. Apart from that, the precise detection of the modulated part of every chirp used for the communication, is highly reliant on the accurate alignment of the carrier frequency of the communication receiver at the CaCS receiving node. Since the parameters adopted from current automotive radar sensors can differ at the transmitter side dependent on the automotive supplier, the carrier alignment of the communication receiver of the CaCS node might not concur with the one in the CaCS transmitter, as shown in Fig. 3. The aforementioned misalignment frequency $\Delta f_{\mathrm{drift}} = f_{\mathrm{Com,Tx}} - f_{\mathrm{Com,Rx}}$ will lead to an explicit failure during the demodulation. As a result, the transmitted data will not be detected correctly.

3. SYNCHRONIZATION FOR COMMUNICATION-ASSISTED CHIRP SEQUENCE

The frame structure showing the transmit signal for the proposed CaCS system is depicted in Fig. 4. The transmitting frame contains the chirps $q_{\mathrm{s}} \in \{0, 1, \ldots, Q_{\mathrm{s}} - 1\}$ split into two sections for synchronization and communication. As determined by Fig. 4, every CaCS-node that aims to communicate with

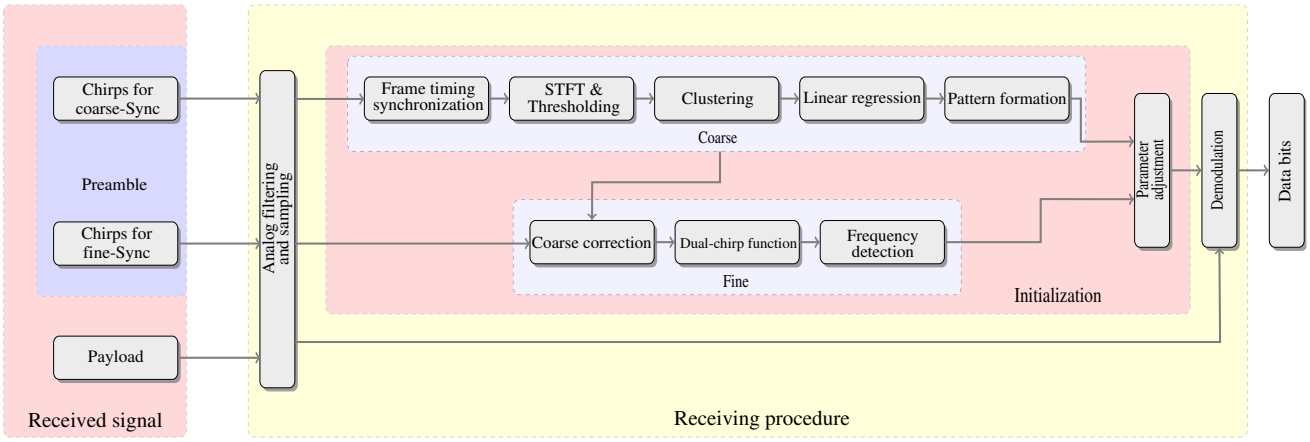

Figure 5. Receiving procedure of the communication receiver including the steps of the synchronization method and the demodulation. The first chirps are responsible for the synchronization, while others convey radar-communication data.

other nodes, i.e., radar sensors, in the environment should predetermine at least multiple chirps for synchronization purposes. This structure is adopted for CaCS-nodes that depend on the chirp scheme for the radar measurements, and it might differ related to the assigned waveform. The chirps dedicated for synchronization can be divided into two groups for dealing with coarse and fine time-frequency shifts. The aforementioned chirps are sets of up-down chirps (for example, 16 predetermined sets) with index $q_{\mathrm{sync}} \in \{0, 1, \ldots, Q_{\mathrm{sync}} - 1\}$, where $(Q_{\mathrm{sync}} < Q_{\mathrm{s}}) \in \mathbb{N}_{+}$. The synchronization sets are predetermined as a preamble at the beginning of the transmission and play a significant role to realign the receiver in the time-frequency plane correctly. Although the mentioned pattern is equivalent to the classical FMCW dual-ramps waveform, the investigated signal lasts a shorter period (e.g., $T_{\mathrm{C,com}} = T_{\mathrm{C,sync}} = 50\,\mu\mathrm{s}$ for automotive radars with $B = 1\,\mathrm{GHz}$ at the 77–81 GHz band). In addition, the last two sets of up-down chirps are assigned for performing the fine synchronization. The fine synchronization chirps play a vital role in the proposed algorithm to correct residual time and frequency offsets that were not fully compensated in the former stage. Next, Fig. 4 shows the CaCS chirps $Q_{\mathrm{rc}} < Q_{\mathrm{s}}$ adopted for both radar measurements and communication evaluation at the receiver of another CaCS-node. Although the aforementioned method follows the integration method described in [29] and depicted in Fig. 4, it can be adapted for other CaCS systems [38, 39].

4. RECEIVING PROCEDURE

This section describes the chosen receiving procedure to extract the communication data at the receiver side of a CaCS node. The receiving procedure consists of an initialization section and a demodulation process, as depicted in Fig. 5. The initialization ensures the time-frequency alignment of the signal at the communication receiver side by performing both coarse and fine synchronizations. A sliding-window approach reliant on Schmidl and Cox is assigned to detect the beginning of the preamble. Next, the unknown signal pattern transmitted from CaCS-nodes is estimated based on STFT and linear regression as an adaptation of image processing. In addition, the demodulation is performed on the received modulated chirps to retrieve the communication data. Assuming the described structure of CaCS signal, the receiving procedure shown in Fig. 5 contains multiple sections. The first section, which is transmitted from one CaCS-node, is dedicated for synchronization, while the next part carries the radar-communication data.

4.1. Coarse Synchronization

As indicated in the previous section, the assumed communication receiver has a limited frequency bandwidth, on the one hand, to keep the adjustment equivalent to the hardware adopted in current chirp

sequence radar sensors. On the other hand, the bounded frequency bandwidth limits the hardware costs compared with the digital radar systems, which require fast ADCs. However, since the current radar sensors can adopt various unknown parameters, such as center frequency and time durations, within the same frequency bandwidth, the demodulation process might fail without a guaranteed synchronization between the transmitter and receiver. In this study, the coarse synchronization is intended to amend the time and frequency offsets that occurred at the communication receiver of one CaCS-node. The structure and functions of the coarse synchronization are depicted in Fig. 5 and explained in the following.

4.1.1. Frame Timing Synchronization

The considered chirps assigned for coarse synchronization are filtered (e.g., $B_{\mathrm{Com}} = 10\,\mathrm{MHz}$) at the receiver so that only a part of the received CaCS signal is sampled by ADC and processed further. The start of the preamble appointed for synchronization is determined with a sliding window derived from Schmidl and Cox algorithm [21]. The sliding window is divided into two sections that will be correlated to create a peak at the start of the preamble. If $2U$ presents the length of the preamble in samples, the correlation between the two assigned sections is given by

$$AC[z] = \sum_{v=0}^{U-1} s^*_{z+v} s_{z+v+U} \tag{3}$$

where z is the sample index related to the sliding window. In this context, the metric of the correlation process scaled by the received energy of the second half-preamble MC is performed as

$$ME[z] = \frac{|AC(z)|^2}{(MC(z))^2} \tag{4}$$

where the energy of the preamble is calculated as

$$MC[z] = \sum_{v=0}^{U-1} |s_{z+v+U}|^2. \tag{5}$$

Figure 6 illustrates the output of the correlator caused by the shift during the transmission for different values of delay τ based on the length of the preamble $2U$. The maximum value of the correlator indicates the start position of the preamble t_{start}, and the pattern formulated by the correlation has its shape according to the specifications of chirp signals.

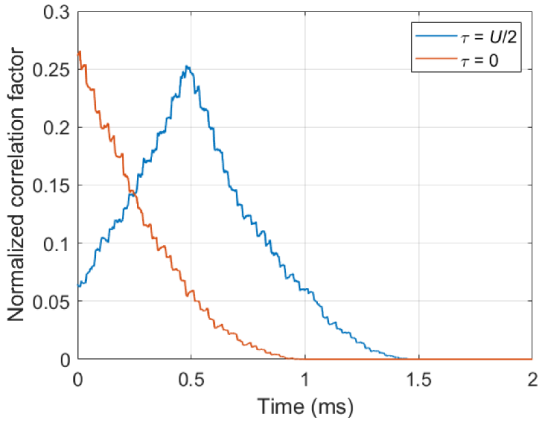

Figure 6. Exemplary coarse timing estimation related to the start point of the preamble.

4.1.2. STFT and Thresholding Based Image Signal Processing

After indicating the start point of the preamble in the previous paragraph, the filtered signal is analyzed by STFTs in the time-frequency plane as adaptation of image signal processing. STFT is an adjustment

of the discrete Fourier transform (DFT), where the signal is divided into multiple segments of an adequate length M and multiplied with a chosen windowing function $w[n]$ of length $N \in \mathbb{N}$ [40, 41], (for instance, Hamming). The discrete equation representing the filtered signal after applying the STFT can be expressed as

$$S_{q_c}[m,k] = \sum_{n=0}^{N-1} s[n+mP]\; w[n]\; \exp\left[\frac{-2\mathrm{j}\pi kn}{N}\right] \tag{6}$$

with $m \in \mathbb{Z}$ being the segment index, $n \in [0, N-1]$ the sample index, and $P \in \mathbb{N}$ the STFT hope size. $k \in [0, K]$ is the frequency index, and $q_c \in \{0, 1, \ldots, Q_c - 1\}$ is the chirp index that indicates the coarse synchronization chirps, where $Q_c < Q_{\text{sync}} < Q_s$. Fig. 7(a) shows an exemplary received signal after filtering it and applying the STFT. Since only a part of the signal is sampled, the signal is visualized within the MHz scope in Fig. 7. Next, a thresholding function $\gamma(a)$ to separate noise and chirps is applied on S_{q_c} as

$$\gamma(a) = \begin{cases} 0 & \text{if } |a| \le H \\ a & \text{if } |a| > H \end{cases} \tag{7}$$

where H is empirically set related to the value of the signal-to-noise ratio (SNR) of the received signal, i.e., all elements of the time-dependent power spectral density (PSD) of the signal less than H are set to zero. Setting H influences the density of the points after applying the STFTs so that the complexity

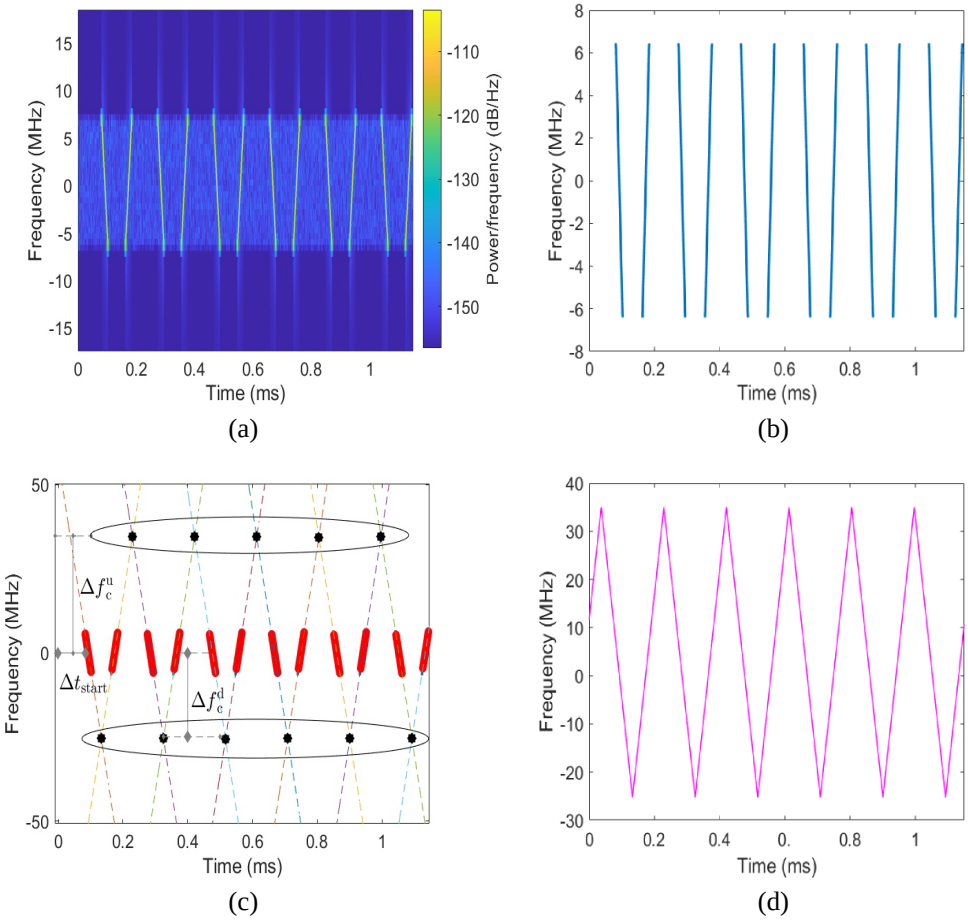

Figure 7. Visulaization of the coarse synchronization signal under the proposed method where the filtered signal at the receiver side conclude solely a part of the complete bandwidth. (a) Spectrogram of the signal using STFT. (b) The time-frequency plane of the signal after thresholding and clustering. (c) Intersections finder based on linear regression. (d) Chirp pattern after applying pattern formation related to the intersections finder.

of the calculation becomes lower. If a low value of H is set, the number of allocated points increases, leading to more complexity in assigning the clusters and a deviation in the linear regression afterward. The signal S_{q_c} after applying the thresholding is given as

$$S_{q_c}^{\gamma}[m,k] = \gamma(S_{q_c}[m,k]) \tag{8}$$

and further processed in the following steps.

4.1.3. Clustering

A clustering method can be implemented to reduce the influence of noise on the investigated signal so that the signal pattern can be efficiently estimated in the next step. One algorithm adopted in this study is density-based spatial clustering of applications with noise (DBSCAN) [42]. DBSCAN relies on a density-based notion of clusters and has the advantage that no *a priori* input about the number of clusters is required. The algorithm input includes the following data: The output matrix of the thresholding operation after the STFTs, the minimum number of neighbors $N_{\min} \in \mathbb{N}_+$ required for a core point, and the radius for a neighborhood search $\epsilon \in \mathbb{R}_+$ around the point. A point p is directly density-reachable from another point v with respect to ϵ, $N_{\min}$, and a dataset $\{(x,y)_{q_c}^{\gamma}\}$ if

- $Eps(p) = \{v \in \{(x,y)_{q_c}^{\gamma}\} | dist(p,v) \leq \epsilon\}$, and
- $|Eps(p)| \geq N_{\min}$.

where *dist* is the measured distance between the points, and $\{(x,y)_{q_c}^{\gamma}\}$ represents the points in the time-frequency plane of the investigated signal $S_{q_c}^{\gamma}$. As soon as the clusters are defined and set together to create the linear structure of the received chirps, the next step will be responsible for predicting the signal pattern. Fig. 7(b) depicts the signal after applying the thresholding and clustering consequently, and a brief explanation of DBSCAN is summarized in Algorithm 1.

4.1.4. Linear Regression

The key idea of reconstructing the transmit chirp subsequence is to estimate the slope of every up- and down-chirp within the mentioned synchronization section to derive the complete transmit pattern.

Algorithm 1: DBSCAN algorithm.

```
Input: {(x,y)^γ_qc}, N_min, ϵ, C_cluster ← 0
for each point p ∈ {(x,y)^γ_qc} do
    if p is unclassified then
        the lable of clusters C_cluster = C_cluster + 1
        for each point v ∈ {(x,y)^γ_qc} do
            if dist(p,v) ≤ ϵ then
                p is directly density-reachable from v
                v is a neighbor point
                if |Eps(p)| ≥ N_min then
                    p is a core point
                else
                    p is a noise point
                end
            else
                select another point
            end
        end
    else
        select another point
    end
end
Output: {(x,y)^γ_qc} according to C_cluster
```

Given the output of the previous step, the slope of the chirps within the investigated dataset $\{(x,y)^{\gamma}_{q_c}\}$ is computed. The calculation depends on linear regression (least-squares approximation), as described in [43]. The linear regression problem is to be solved by the following linear equation

$$y = \mu^{\gamma}_{q_c} x + c^{\gamma}_{q_c} \tag{9}$$

where $\mu^{\gamma}_{q_c}$ is the slope of the line, and $c^{\gamma}_{q_c}$ is the y-intercept value. Given a set of points $\{(x,y)^{\gamma}_{q_c}\}$ in the time-frequency plane, there is a line $\hat{y} = \hat{\mu}^{\gamma}_{q_c} x + \hat{c}^{\gamma}_{q_c}$ that best qualifies the data in terms of minimizing the root mean square (RMS) error, where $\hat{\mu}^{\gamma}_{q_c}$ can be calculated as

$$\hat{\mu}^{\gamma}_{q_c} = \frac{\sum_{l=0}^{L-1}(x_l - \overline{x})(y_l - \overline{y})}{\sum_{l=0}^{L-1}(x_l - \overline{x})^2} \tag{10}$$

with $\overline{y}$ and $\overline{x}$ denoting the mean of the chosen time-frequency plane points. $l \in \{0, 1, \ldots, L-1\}$ is the index related to the points of the investigated dataset $\{(x,y)^{\gamma}_{q_c}\}$, which represents the time-frequency plane in this study. In addition, $\hat{c}^{\gamma}_{q_c}$ can be derived from

$$\hat{c}^{\gamma}_{q_c} = \overline{y} - \hat{\mu}^{\gamma}_{q_c} \overline{x} \tag{11}$$

The output of the linear regression is a set of linear lines corresponding to the investigated datasets $\{(x,y)^{\gamma}_0, \ldots, (x,y)^{\gamma}_{q_c-1}, (x,y)^{\gamma}_{q_c}, (x,y)^{\gamma}_{q_c+1}, \ldots\}$ as shown in Fig. 7(c). Since the transmitting chirps are linear and well predetermined, every consequent up-down chirp, as well as down-up chirp, will intersect at a certain point in the time-frequency plane, which will contain all intersections between the analyzed up-down chirps. From this perspective, every intersection (top- or down-seeded) between every two successive chirps is given by solving the two linear equations

$$y = \hat{\mu}^{\gamma}_{q_c} x + \hat{c}^{\gamma}_{q_c}, \tag{12}$$

$$y = \hat{\mu}^{\gamma}_{q_c+1} x + \hat{c}^{\gamma}_{q_c+1} \tag{13}$$

Next, the up- and down-seeded intersections between the chirps are attained. The solution includes one set of coordinates within the intersections chain $\{(\hat{X},\hat{Y})^{\gamma}_0, (\hat{X},\hat{Y})^{\gamma}_1, ..., (\hat{X},\hat{Y})^{\gamma}_{Q_c-1}\}$. $(\hat{X},\hat{Y})^{\gamma}_{q_c}$ represents the intersection coordinates in the time-frequency plane, and q_c is the chirp index. The up-seeded frequency offset Δf^{u}_{c} is derived from the mean value of the upper intersections black-marked along the Y-axis as shown in Fig. 7(c)

$$\Delta f^{u}_{c} = \frac{2}{Q_c} \sum_{q_c=0}^{Q_c/2-1} \hat{Y}^{\gamma}_{2q_c} \tag{14}$$

while the down-seeded frequency offset Δf^{d}_{c} can be derived from the mean value of the lower intersections along the Y-axis as shown in Fig. 7(c)

$$\Delta f^{d}_{c} = \frac{2}{Q_c - 2} \sum_{q_c=0}^{Q_c/2-2} \hat{Y}^{\gamma}_{2q_c+1} \tag{15}$$

As a result, the sequence pattern is reconstructed (pattern formation in Fig. 7(d)) in the time-frequency plane, and the carrier frequency $f_{\mathrm{Com,Rx}}$ at the receiver side of the investigated CaCS-node is retuned dependent on the distance between the intersections and the communication part. The mentioned distance above should be known so that the former process does not lead to further undesired misalignments.

The complexity of the proposed method depends mainly on the STFT and linear regression after indicating the beginning of the frame. The detection of the start point is equivalent to the complexity of applying a matched filter related to the correlation. For each STFT process, the computational complexity is given by $M \times \mathcal{O}(N \log N)$, where N is the length of the assigned window, and M represents

the number of FFT operations (number of segments) employed to calculate STFT. In addition, for clustering, $\mathcal{O}(F \log F)$ operations are needed in the best case, where F represents the number of the scanned points. On the other hand, for each linear regression operation after thresholding $\mathcal{O}(R^3)$ is required, where R is the number of features in the normal equation of the linear regression. A short explanation of the coarse synchronization is summarized in Algorithm 2.

Algorithm 2: Coarse synchronization algorithm.

Detection of the start point $\rightarrow$ (3) and (4) $\rightarrow t_{\text{start}}$
Image-like processing
  Input: S_{q_c}
  for *each up-down chirp within the coarse synchronization sub-sequence* **do**
    compute STFT to obtain $S_{q_c}[m,k]$
    set a threshold H for the samples $\rightarrow S_{q_c}^{\gamma}[m,k] = \gamma(S_{q_c}[m,k])$
    extract the data and set them together after clustering (Algorithm 1 $\rightarrow \{(x,y)_{q_c}^{\gamma}\}$)
    compute both $\hat{\mu}_{q_c}^{\gamma}$ and $\hat{c}_{q_c}^{\gamma}$ $\rightarrow$ (10) and (11)
  end
  calculate the up- and down-seeded intersections between every two successive chirps $\rightarrow$ (12), and (13)
  extract $(\hat{X},\hat{Y})_{q_c}^{\gamma}$ of every up- and down-seeded intersection
  calculate $\Delta f_{\text{c}}^{\text{u}}$ and $\Delta f_{\text{c}}^{\text{d}}$ $\rightarrow$ (14) and (15)
Output: $\Delta f_{\text{c}}^{\text{u}}$ and $\Delta f_{\text{c}}^{\text{d}}$

4.2. Fine Synchronization

Since the bandwidth used in automotive applications can span over 1 GHz or even above, the time and frequency shifts might be considerable and cause some failures during the demodulation of communication data. Although the coarse synchronization in the preceding subsection can estimate and correct the occurred offsets in the time-frequency plane, and the method is bounded by the minimum RMS error caused during the estimation of the slopes. These additional offsets are usually small, but they might influence the demodulation process; therefore, they should be compensated. Fig. 8 illustrates an exemplary signal created at the communication receiver (R_{ref}, blue-marked) for downconversion that should match the receiving counterpart (Rx, red-marked) if the investigated signals are fully synchronized. As described previously in this section, this approach mainly relies on employing a set of an up- and a down-chirp to estimate two residual frequencies equivalent to the range-Doppler estimation in FMCW radar [44]. The aforementioned frequency offset between the investigated nodes related to the fine stage can be defined as

$$\Delta f_{\text{f}} = \frac{f_2 - f_1}{2} \tag{16}$$

and the corresponding time offset can be derived from

$$\Delta t_{\text{f}} = \frac{f_2 + f_1}{2\mu} \tag{17}$$

where μ is the chirp rate, and f_1, f_2 are the respective residual frequencies related to the up- and down-chirps after the downconversion and applying of the discrete Fourier transform (DFT) successively. It is worth highlighting that the mentioned fine synchronization concept is hard to be executed without any previous coarse synchronizations or GPS due to the broadly utilized bandwidth in automotive applications (1 GHz or more). Moreover, the receiver of the investigated CaCS-node must consecutively generate an up- and a down-chirp, which might be digitally performed after the CW downconversion related to the communication carrier frequency. A brief description of the fine synchronization is introduced in Algorithm 3.

Algorithm 3: Fine synchronization algorithm.

1 Adopt the correction results from the coarse synchronization
2 Filter the chirps according to the investigated bandwidth, and convert the signal to the digital domain
3 **for** *set of an up- and a down chirp within the joint radar-communication sequence* **do**
4 | Downconvert the chirps according to FMCW concept (downcoversion with a reference set of up- and down-chirps)
5 | compute DFT to attain both f_1, $f_2 \rightarrow$ (16) and (17)
6 **end**
7 **Output**: Δf_f, and Δt_f

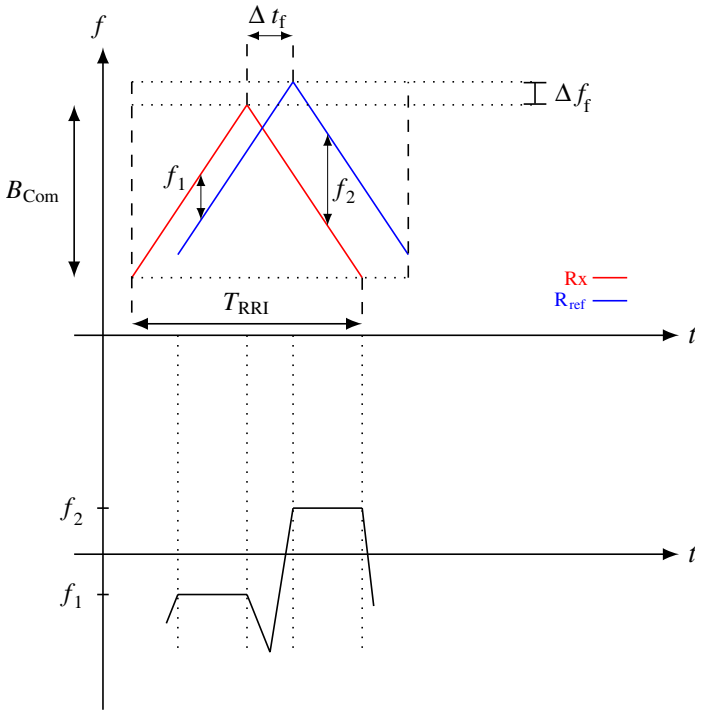

Figure 8. Residual misalignment between two exemplary signals at the communication receiver related to the fine stage.

4.3. Demodulation

After correcting the receiver alignment of the investigated CaCS-node in the time-frequency plane (i.e., the prediction of the transmit signal pattern), the demodulation can be applied to extract the transmit communication data. A detailed description of the demodulation can be found in [29], where the study investigated the partial chirp modulation with various digital modulation schemes (e.g., FSK, PSK). It is worth highlighting that a part of the transmitting chirp has been used as another preamble to detect the beginning of the communication section transmitted from one CaCS-node.

4.4. Multi-User Scenario with Mutual Interference

In the previous subsections, the proposed method for synchronization has been presented. The transmitter and receiver can exchange the information after assuring the synchronization procedure. However, a typical automotive environment includes many radar sensors that can work within the same bandwidth and time duration, leading to interference between the signals and affecting the radar performance [45]. Since the proposed communication method in [29] carries the data partially (e.g.,

on 10% of the radar bandwidth B), the probability of interference over the communication section can be limited. Besides, only a fraction of the coexisting signals N_i within the radar bandwidth B influence communication symbols carried within the B_{Com}. One critical issue concerning the proposed synchronization method is the clustering and linear regression applied to estimate the exact slope of the signal. If the number of the investigated overlapping signals increases, the algorithm undergoes imprecision in inferring the desired signal pattern because of the increasing error related to the linear regression. Section 5 presents the capability of the proposed synchronization method to create the desired pattern when multi-signals are carried within the whole bandwidth B of the radar-communication signal. Although the proposed synchronization method is applied to decentralized systems due to the lack of regulations between the manufacturers of radar sensors, centralized scheduling [5] can be adapted to coordinate the radar sensors if a standardization system can be confirmed.

5. MEASUREMENT SETUP AND SIMULATION RESULTS

In this section, the measurement setup demonstrating the proposed synchronization method is introduced for communication purposes between CaCS nodes. The suggested concept has been investigated using two completely unsynchronized Universal Software Radio Peripherals (USRPs) of type X310 from Ettus Research to represent two CaCS-nodes, SubMiniature version A cable (SMA), and attenuators as depicted in Fig. 9(a). Moreover, the chosen frequency carrier on the receiver is manually assigned to deviate $B/4$ from its counterpart at the transmitter side of one CaCS-node to ensure signal misalignment. It is worth highlighting that a random offset is either added or subtracted from the assigned deviation related to the USRPs [46], which are used for the investigation as a proof of concept with band-limited DACs and ADCs. Additionally, the analog filtering in Fig. 5 was replaced with a digital counterpart in Matlab with down-sampling to achieve the desired limited bandwidth of the received signal. Using the parameters performed in Table 1, the coarse frequency difference shown in Fig. 9(b) ($\Delta f_{\text{Sync}} = f_{\text{C,Tx}} - f_{\text{C,Rx}} - f_{\text{offset}} \simeq 8.125\,\text{MHz}$) is estimated with the coarse synchronization chirps, where f_{offset} is a random offset value related to the USRPs. The start point of the preamble is detected according to the approach suggested in Section 4.1.1 to $(t_{\text{start}} \cdot f_s) \simeq 2480\,\text{Samples}$. Fig. 7 depicts the visualization of the coarse synchronization chirps in accordance to Algorithm 2 in Section 4. Besides, Figs. 7(a) and (b) show the coarse synchronization chirps in the time-frequency plane after filtering and applying both thresholding and clustering w.r.t Algorithm 1. Next, the slope of every up- and down-chirp is estimated relying on the linear regression analysis presented in (10) and (11).

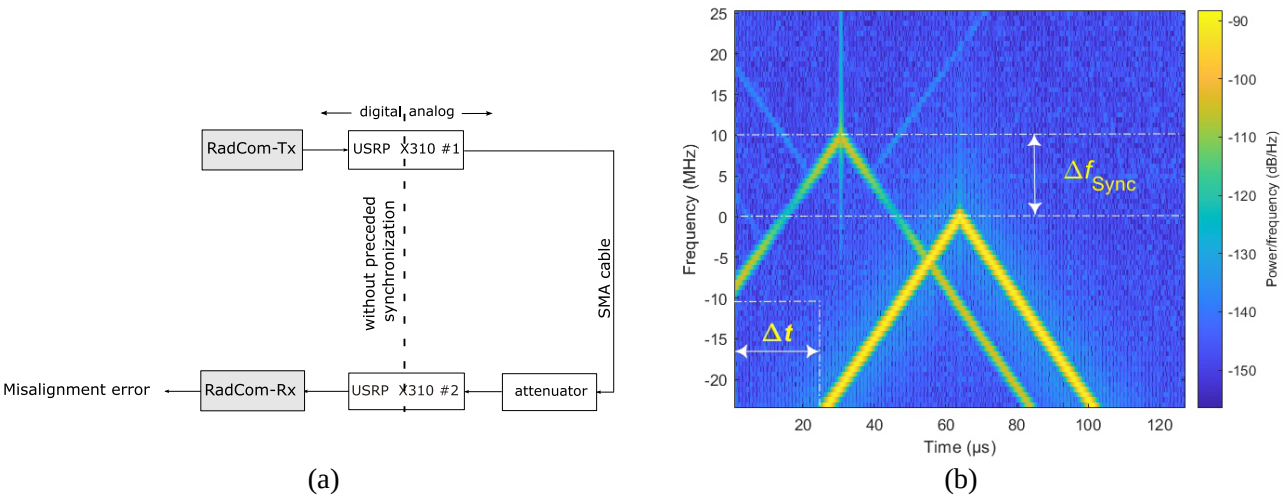

Figure 9. Measurement setup demonstrating the investigated transmit and receive signals. (a) Measurement setup using two USRPs, SMA cable and attenuators. (b) The transmit and receive signals through the measurement before applying the proposed synchronization algorithm.

Table 1. Parameters of the measurement setup and simulations.

Symbol	Parameter	Value
B	Chirp bandwidth	40 MHz
f_{S}	Sampling frequency	80 MHz
$f_{\mathrm{C,Tx}}$	Transmitter carrier frequency	4.05 GHz
$f_{\mathrm{Com,Tx}}$	Communication frequency	4.075 GHz
$f_{\mathrm{C,Rx}}$	Receiver carrier frequency	4.04 GHz
T_{C}	Ramp duration	64 µs
T_{RRI}	Ramp repetition interval	192 µs
Q_{c}	No. of evaluated chirps	16
ϵ	Radius of clusters	2.5
N_{min}	No. of neighboring points	5

Furthermore, the output of the intersections finder related to (14) and (15) is shown in Fig. 7(c), where the up- and down-seeded intersections are plotted as black-marked points between the diagonal lines. After analyzing the output of all mentioned steps, the sequence pattern is designed and reconstructed as depicted in Fig. 7(d), and $\Delta f_c^u \simeq 22.06\,\mathrm{MHz}$, $\Delta f_c^d \simeq -38.3\,\mathrm{MHz}$ are determined. After that, the time-frequency alignment of the receiver is reallocated, and the fine synchronization scheme is carried out dependent on Algorithm 3 in Section 4. As a result, the two residual frequency shifts are estimated according to the range-Doppler concept. The corresponding fine frequency offset is calculated as $\Delta f_f = (f_2 - f_1)/2 = 12\,\mathrm{kHz}$, and the fine time offset is $\Delta t_f \cdot f_s = (f_2 + f_1) f_s/(2\mu) = 192\,\mathrm{Samples}$, as shown in Fig. 10. It is worth highlighting that almost any chirp modulation can be adopted reliant on the mentioned method. Nevertheless, the recommended communication approach is equivalent to the partial chirp communication [29].

Moreover, the influence of the signal-to-noise ratio (SNR) is investigated via simulations with the same parameters adopted during the measurement, as illustrated in Fig. 11. The linear regression employed on the receive signal cannot extract the signal pattern if the investigated signal has low SNR, which leads to a failure related to the inaccurate alignment between the transmitter of one CaCS-node and the receiver of another node, and influences the fine synchronization. Although the clustering can mitigate the influence of noise, the coarse synchronization might generate a wrong signal pattern

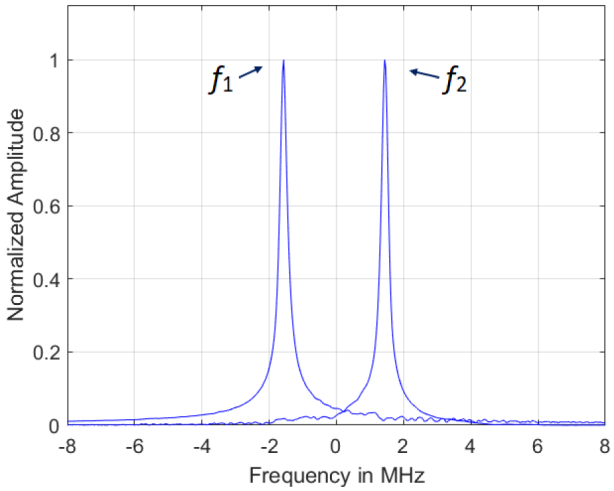

Figure 10. Frequency shifts related to the fine synchronization stage based on the range-Doppler estimation in FMCW radars.

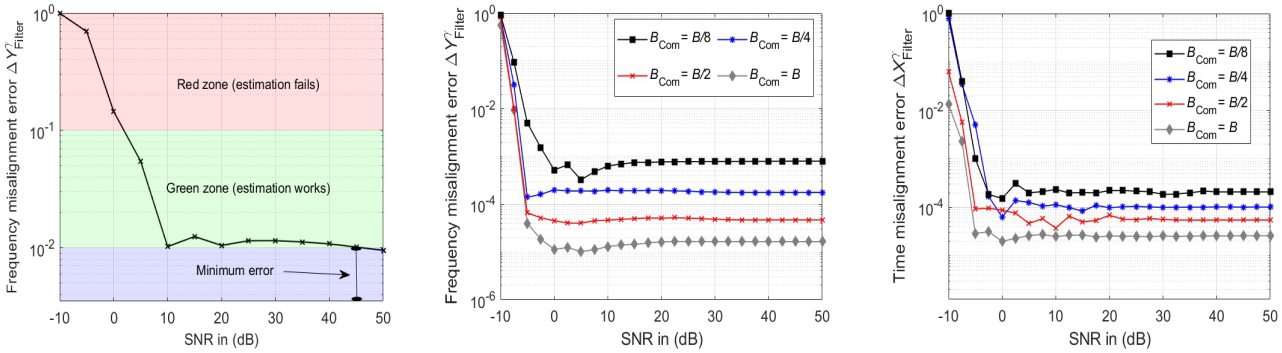

(a) (b) (c)

Figure 11. Simulation results of the coarse synchronization verification. (a) The frequency misalignment error dependent on SNR for $B_{\text{Com}} = B/20$. (b) Simulated frequency misalignment error related to different communication bandwidths $B_{\text{Com}} = \{B/8, B/4, B/2, B\}$. (c) Simulated time and frequency misalignment errors related to different communication bandwidths.

when the noise level increases. Fig. 11(a) depicts the estimated frequency error related to the coarse synchronization dependent on the SNR level. The blue zone illustrates the minimum error achieved based on the minimum square error within the linear regression applied on the receiving signal after the STFT, thresholding, and clustering. Besides, the green field represents the zone where the proposed scheme can correct the occurred failure. However, the green section might differ based on the designed system (in Fig. 11(a), was chosen related to a filter that possesses 5% of the broad bandwidth adopted in the system). On the other hand, the red zone illustrates the section where the synchronization fails to correct the receiver misalignment. Nevertheless, the red zone can be minimized by adopting a filter with higher bandwidth. The indicated relative frequency misalignment can be calculated as

$$\Delta Y^{\gamma}_{\text{Filter}} = \left(\frac{Y^{\gamma}_{\text{Filter}} - \hat{Y}^{\gamma}_{\text{Filter}}}{Y^{\gamma}_{\text{Filter}}} \right) \tag{18}$$

where $Y^{\gamma}_{\text{Filter}}$ is the right frequency alignment and $\hat{Y}^{\gamma}_{\text{Filter}}$ the estimated counterpart. Furthermore, Fig. 11(b) depicts the frequency misalignment error related to different bandwidths analyzed on the communication receiver of one CaCS-node. For $B_{\text{Com}} = B/8$ is the minimum achieved misalignment error $\Delta Y^{\gamma}_{\text{Filter}} \simeq 7 \times 10^{-4}$, while using a wider bandwidth (e.g., $B_{\text{Com}} = B/2$) $\Delta Y^{\gamma}_{\text{Filter}}$ is located around 7×10^{-5}. On the other hand, Fig. 11(c) presents the estimated time error $\Delta X^{\gamma}_{\text{Filter}}$ of the proposed synchronization method dependent on different values of the investigated bandwidth assigned at the communication receiver of one CaCS-node. The relative time misalignment can be calculated as

$$\Delta X^{\gamma}_{\text{Filter}} = \left(\frac{X^{\gamma}_{\text{Filter}} - \hat{X}^{\gamma}_{\text{Filter}}}{T_{\text{RRI}}} \right) \tag{19}$$

where $X^{\gamma}_{\text{Filter}}$ is the right time alignment and $\hat{X}^{\gamma}_{\text{Filter}}$ the estimated counterpart, and the aforementioned misalignment is normalized by T_{RRI} and located around 10^{-4} for $B_{\text{Com}} = B/4$. It is worth highlighting that the performance achievable with the proposed algorithm in Fig. 10 and Fig. 11 highly depends on the steps applied for the coarse synchronization, including the filtering, where the density of the points of the receiving signal filtered after the downconversion increases with higher SNR leading to saturating the error curves around particular values in Fig. 10 and Fig. 11.

Apart from that, Fig. 12 illustrates the capability of the proposed synchronization method to recreate the desired signal pattern despite the coexistence of other signals in the surroundings. The simulations are applied depending on the number of coexisting signals N_i carried within the whole bandwidth B of the radar-communication system, as depicted in Fig. 12(a). Since the proposed method employs a partial bandwidth B_{Com} to estimate the desired signal pattern, the probability that the coexisting signals deteriorate the algorithm is limited. The cumulative distribution function (CDF)

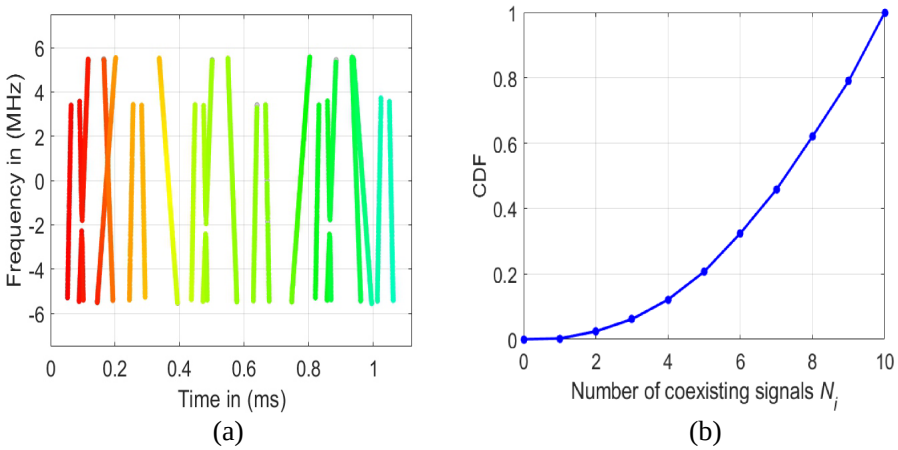

Figure 12. Simulation results for the CDF regarding synchronization failures in multi-user scenarios. (a) Exemplary cluster allocations in a scenario with multiple coexisting signals. (b) CDF reliant on the number of coexisting signals within the complete bandwidth of the system.

represents the cumulative misalignment of the wrong pattern formation (failure of synchronization), as shown in Fig. 12(b), where not every coexisting signal transmitted within the bandwidth B should interfere with the desired signal in B_{Com}. In light of the linear regression described in Section 4.1.4, the pattern formation, in this case, also depends on the distance assessment between the up- and down-seeded intersections in Fig. 7(c).

6. CONCLUSION

A preamble-based synchronization method for a CaCS system has been proposed in this paper. Since the parameters adopted from current automotive radar sensors can differ at the transmitter side dependent on the automotive supplier, the carrier alignment of the communication receiver of the CaCS node might not concur with the one in the CaCS transmitter. The suggested approach relies on a novel coarse synchronization method that includes a sliding correlation procedure based on Schmidl & Cox algorithm to estimate the start point of the preamble. Next, image-like processing (constituted by STFT, clustering, and linear regression) is used to estimate frequency offsets between the transmitter of a CaCS-node and the communication receiver of another node. Also, a fine synchronization method has been investigated equivalent to the range-Doppler estimation in FMCW radars to correct additional time and frequency offsets that have not been corrected during the coarse stage. A measurement setup using two completely unsynchronized USRPs was performed to validate the proposed method. As a proof of concept, the occurring time and frequency offsets were corrected in two stages, and the communication receiver was realigned in the time-frequency plane to recover the communication data. Although only the synchronization of two independent CaCS-nodes has been measured, the proposed method is further investigated for multi-user scenarios. Due to the narrow bandwidth adopted in the synchronization step, other signals in the surroundings have a limited effect on the proposed method.

ACKNOWLEDGMENT

This work was supported in part by the German Federal Ministry of Education and Research (BMBF) through IMIKO-Radar Project under Grant 16EMO0343.

REFERENCES

1. Roos, F., J. Bechter, C. Knill, B. Schweizer, and C. Waldschmidt, "Radar sensors for autonomous driving: Modulation schemes and interference mitigation," *IEEE Microw. Mag.*, Vol. 20, No. 9, 58–72, 2019.

2. Hakobyan, G. and B. Yang, "High-performance automotive radar: A review of signal processing algorithms and modulation schemes," *IEEE Signal Process. Mag.*, Vol. 36, No. 5, 32–44, 2019.
3. Waldschmidt, C., J. Hasch, and W. Menzel, "Automotive radar — From first efforts to future systems," *IEEE J. Microw.*, Vol. 1, No. 1, 135–148, 2021.
4. Bechter, J., F. Roos, M. Rahman, and C. Waldschmidt, "Automotive radar interference mitigation using a sparse sampling approach," *Proc. Eur. Radar Conf. (EURAD)*, 90–93, 2017.
5. Aydogdu, C., M. F. Keskin, N. Garcia, H. Wymeersch, and D. W. Bliss, "Radchat: Spectrum sharing for automotive radar interference mitigation," *IEEE Trans. Intell. Transp. Sys.*, Vol. 22, No. 1, 416–429, 2021.
6. Aydogdu, C., M. F. Keskin, G. K. Carvajal, O. Eriksson, H. Hellsten, H. Herbertsson, E. Nilsson, M. Rydstrom, K. Vanas, and H. Wymeersch, "Radar interference mitigation for automated driving: Exploring proactive strategies," *IEEE Signal Process. Mag.*, Vol. 37, No. 4, 72–84, 2020.
7. Al-Hourani, A., R. J. Evans, S. Kandeepan, B. Moran, and H. Eltom, "Stochastic geometry methods for modeling automotive radar interference," *IEEE Transactions on Intelligent Transportation Systems*, Vol. 19, No. 2, 333–344, 2018.
8. *IEEE Veh. Tech. Mag., Special Issue on V2V Communications 2(4)*, Dec. 2007.
9. Karagiannis, G., O. Altintas, E. Ekici, G. Heijenk, B. Jarupan, K. Lin, and T. Weil, "Vehicular networking: A survey and tutorial on requirements, architectures, challenges, standards and solutions," *IEEE Communications Surveys Tutorials*, Vol. 13, No. 4, 584–616, 2011.
10. 3GPP, Service requirements for enhanced V2X scenarios (3GPP TS 22.186 version 15.3.0 Release 15), 2020.
11. IEEE, "IEEE Standard for Information technology — Local and metropolitan area networks — Specific requirements — Part 11: Wireless LAN Medium Access Control (MAC) and Physical Layer (PHY) Specifications Amendment 6: Wireless Access in Vehicular Environments," IEEE Std 802.11p-2010 (Amendment to IEEE Std 802.11-2007), 1–51, 2010.
12. Manolakis, K. and W. Xu, "Time synchronization for multi-link D2D/V2X communication," *Proc. IEEE 89th Veh. Technol. Conf. (VTC-Fall)*, 1–6, 2016.
13. ETSI, Intelligent Transport Systems (ITS); Performance Evaluation of Self-Organizing TDMA as Medium Access Control Method Applied to ITS; Access Layer Part, 2011–2012.
14. Sturm, C. and W. Wiesbeck, "Waveform design and signal processing aspects for fusion of wireless communications and radar sensing," *Proc. IEEE*, Vol. 99, No. 7, 1236–1259, 2011.
15. De Oliveira, L. G., B. Nuss, M. B. Alabd, A. Diewald, M. Pauli, and T. Zwick, "Joint radar-communication systems: Modulation schemes and system design," *IEEE Trans. Microw. Theory Techn.*, Mar. 2022.
16. Hassanien, A., M. G. Amin, E. Aboutanios, and B. Himed, "Dual-function radar communication systems: A solution to the spectrum congestion problem," *IEEE Signal Process. Mag.*, Vol. 36, No. 5, 115–126, 2019.
17. Sit, Y. L., C. Sturm, T. Zwick, L. Reichardt, and W. Wiesbeck, "The OFDM joint radar-communication system: An overview," *The 3rd Int. Conf. on Adv. in Satell. and Space Commun., SPACOMM 2011*, 69–74, Budapest, Hungary, Apr. 17–22, 2011.
18. Braun, K. M., "OFDM radar algorithms in mobile communication networks," Ph.D. dissertation, Karlsruher Institut für Technologie (KIT), 2014.
19. De Oliveira, L. G., M. B. Alabd, B. Nuss, and T. Zwick, "An OCDM radar-communication system," *2020 14th Eur. Conf. Antennas Propag.*, 1–5, 2020.
20. De Oliveira, L. G., B. Nuss, M. B. Alabd, Y. Li, L. Yu, and T. Zwick, "MIMO-OCDM-based joint radar sensing and communication," *2021 15th Eur. Conf. Antennas Propag.*, 1–5, 2021.
21. Schmidl, T. and D. Cox, "Robust frequency and timing synchronization for OFDM," *IEEE Trans. Commun.*, Vol. 45, No. 12, 1613–1621, 1997.
22. Ouyang, X., "Digital signal processing for fiber-optic communication systems," Ph.D. dissertation, University College Cork, Ireland, 2017.
23. TI, AWR2243 Single-Chip 76- to 81-GHz FMCW Transceiver, 2020.

24. Barrenechea, P., F. Elferink, and J. Janssen, "FMCW radar with broadband communication capability," *Proc. Eur. Radar Conf. (EURAD)*, 130–133, 2007.
25. Scheiblhofer, W., R. Feger, A. Haderer, and A. Stelzer, "Method to embed a data-link on FMCW chirps for communication between cooperative 77-GHz radar stations," *Proc. Eur. Radar Conf. (EURAD)*, 181–184, 2015.
26. Lampel, F., R. F. Tigrek, A. Alvarado, and F. M. Willems, "A performance enhancement technique for a joint FMCW RadCom system," *Proc. Eur. Radar Conf. (EURAD)*, 169–172, 2019.
27. Dwivedi, S., A. N. Barreto, P. Sen, and G. Fettweis, "Target detection in joint frequency modulated continuous wave (FMCW) radar-communication system," *Proc. 16th Int. Symp. on Wireless Commun. Syst. (ISWCS)*, 277–282, 2019.
28. Dwivedi, S., M. Zoli, A. N. Barreto, P. Sen, and G. Fettweis, "Secure joint communications and sensing using chirp modulation," *2nd 6G Wireless Summit (6G SUMMIT)*, 1–5, 2020.
29. Alabd, M. B., B. Nuss, C. Winkler, and T. Zwick, "Partial chirp modulation technique for chirp sequence based radar communications," *Proc. Eur. Radar Conf. (EURAD)*, 173–176, 2019.
30. Lampel, F., F. Uysal, F. Tigrek, S. Orru, A. Alvarado, F. Willems, and A. Yarovoy, "System level synchronization of phase-coded FMCW automotive radars for RadCom," *2020 14th Eur. Conf. Antennas Propag.*, 1–5, 2020.
31. Bernier, C., F. Dehmas, and N. Deparis, "Low complexity lora frame synchronization for ultra-low power software-defined radios," *IEEE Trans. Commun.*, Vol. 68, No. 5, 3140–3152, 2020.
32. Martinez, A. B., A. Kumar, M. Chafii, and G. Fettweis, "A chirp-based frequency synchronization approach for flat fading channels," *2020 2nd 6G Wireless Summit (6G SUMMIT)*, 1–5, 2020.
33. Aydogdu, C., M. F. Keskin, and H. Wymeersch, "Automotive radar interference mitigation via multi-hop cooperative radar communications," *2020 17th European Radar Conference (EuRAD)*, 270–273, 2021.
34. Winkler, V., "Novel waveform generation principle for short-range FMCW-radars," *Proc. German Microw. Conf.*, 1–4, 2009.
35. Kronauge, M. and H. Rohling, "New chirp sequence radar waveform," *IEEE Trans. Aerosp. Electron. Syst.*, Vol. 50, No. 4, 2870–2877, 2014.
36. TI, LMX2491 6.4-GHz Low Noise RF PLL With Ramp/ChirpGeneration, 2017.
37. Winkler, V., "Range doppler detection for automotive FMCW radars," *Proc. Eur. Radar Conf. (EURAD)*, 166–169, 2007.
38. Alabd, M. B., L. G. de Oliveira, B. Nuss, W. Wiesbeck, and T. Zwick, "Time-frequency shift modulation for chirp sequence based radar communications," *Proc. IEEE MTT-S Int. Conf. on Microw. for Intell. Mobility (ICMIM)*, 1–4, 2020.
39. Alabd, M. B., B. Nuss, L. G. de Oliveira, A. Diewald, Y. Li, and T. Zwick, "Modified pulse position modulation for joint radar communication based on chirp sequence," *IEEE Microwave and Wireless Components Letters*, 1–4, 2022.
40. Krawczyk, M. and T. Gerkmann, "STFT phase reconstruction in voiced speech for an improved single-channel speech enhancement," *IEEE/ACM Trans. on Audio, Speech, and Language Process.*, Vol. 22, No. 12, 1931–1940, 2014.
41. Müller, M., *Fundamentals of Music Process*, Springer International Publishing, 2015.
42. Ester, M., H.-P. Kriegel, J. Sander, and X. Xu, "A density-based algorithm for discovering clusters in large spatial databases with noise," *Proc. of the 2nd Int. Conf. on Knowledge Discovery and Data Mining, ser. KDD'96*, 226–231, AAAI Press, 1996.
43. Baglivo, J. A., Mathematica Laboratories for Mathematical Statistics, Society for Industrial and Applied Mathematics, 2005.
44. Vishwanath, T. G., M. Parr, Z.-L. Shi, and S. Erlich, "Synchronization in mobile satellite systems using dual-chirp waveform," Patent, U.S. Patent 6,418,158 B1, Jul. 9, 2002.
45. Torres, L. L. T., F. Roos, and C. Waldschmidt, "Simulator design for interference analysis in complex automotive multi-user traffic scenarios," *IEEE Radar Conf. (RadarConf20)*, 1–6, 2020.
46. Ettus Research. USRP. X300 and X310X Series.